



**HAL**  
open science

## Short echo time dual-frequency MR Elastography with Optimal Control RF pulses

Pilar Sango Solanas, Kevin Tse Ve Koon, Eric Van Reeth, Helene Ratiney, Fabien Millioz, Cyrielle Caussy, Olivier Beuf

► **To cite this version:**

Pilar Sango Solanas, Kevin Tse Ve Koon, Eric Van Reeth, Helene Ratiney, Fabien Millioz, et al.. Short echo time dual-frequency MR Elastography with Optimal Control RF pulses. Scientific Reports, 2022, 12 (1), pp.1406. 10.1038/s41598-022-05262-3 . hal-03563413

**HAL Id: hal-03563413**

**<https://hal.science/hal-03563413>**

Submitted on 9 Feb 2022

**HAL** is a multi-disciplinary open access archive for the deposit and dissemination of scientific research documents, whether they are published or not. The documents may come from teaching and research institutions in France or abroad, or from public or private research centers.

L'archive ouverte pluridisciplinaire **HAL**, est destinée au dépôt et à la diffusion de documents scientifiques de niveau recherche, publiés ou non, émanant des établissements d'enseignement et de recherche français ou étrangers, des laboratoires publics ou privés.

# 1 Short echo time dual-frequency MR Elastography with 2 Optimal Control RF pulses

3  
4 Pilar Sango Solanas<sup>1</sup>, Kevin Tse Ve Koon<sup>1</sup>, Eric Van Reeth<sup>1,2</sup>, Helene Ratiney<sup>1</sup>, Fabien  
5 Millioz<sup>1</sup>, Cyrielle Caussy<sup>3,4</sup> and Olivier Beuf<sup>1\*</sup>

6  
7 <sup>1</sup>Univ Lyon, INSA Lyon, Inserm, UCBL, CNRS, CREATIS, UMR5220, U1294, 69621  
8 Villeurbanne, France

9 <sup>2</sup>CPE Lyon, Département Sciences du Numérique, Lyon, France,

10 <sup>3</sup>Univ Lyon, CarMen Laboratory, INSERM, INRA, INSA Lyon, Université Claude Bernard  
11 Lyon 1, 69495 Pierre-Bénite, France

12 <sup>4</sup>Hospices Civils de Lyon, Département Endocrinologie, Diabète et Nutrition, Hôpital Lyon  
13 Sud, 69495 Pierre-Bénite, France

14

15 **Key words (4):** MR Elastography, multifrequency, Optimal Control theory, RF pulse  
16 design

17

18 **Corresponding author:**

19 Olivier BEUF, PhD

20 CREATIS CNRS UMR 5220

21 INSA Lyon, Bât Léonard de Vinci (401)

22 21 Avenue Jean Capelle

23 F-69621 VILLEURBANNE

24 Tél. +33 4 72 43 85 20

25 [olivier.beuf@creatis.insa-lyon.fr](mailto:olivier.beuf@creatis.insa-lyon.fr)

1 **SUMMARY ABSTRACT**

2

3 Magnetic Resonance Elastography (MRE) quantifies the mechanical properties of tissues,  
4 typically applying motion encoding gradients (MEG). Multifrequency results allow better  
5 characterizations of tissues using data usually acquired through sequential  
6 monofrequency experiments. High frequencies are difficult to reach due to slew rate  
7 limitations and low frequencies induce long TEs, yielding magnitude images with low  
8 SNR.

9 We propose a novel strategy to perform simultaneous multifrequency MRE in the  
10 absence of MEGs: using RF pulses designed via the Optimal Control (OC) theory. Such  
11 pulses control the spatial distribution of the MRI magnetization phase so that the  
12 resulting transverse magnetization reproduces the phase pattern of an MRE acquisition.  
13 The pulse is applied with a constant gradient during the multifrequency mechanical  
14 excitation to simultaneously achieve slice selection and motion encoding. The phase  
15 offset sampling strategy can be adapted according to the excitation frequencies to reduce  
16 the acquisition time.

17 Phantom experiments were run to compare the classical monofrequency MRE to the OC  
18 based dual-frequency MRE method and showed excellent agreement between the  
19 reconstructed shear storage modulus  $G'$ . Our method could be applied to simultaneously  
20 acquire low and high frequency components, which are difficult to encode with the  
21 classical MEG MRE strategy.

22

## 1 1. INTRODUCTION

2 Magnetic Resonance Elastography (MRE) is a valuable non-invasive technique for the  
3 quantification of mechanical properties of tissues based on the measurement of the  
4 characteristics of shear waves propagating through the organ of interest<sup>1</sup>. Many diseases  
5 alter the morphology and structure of the affected organs, producing measurable  
6 modifications of the mechanical properties of tissues. These alterations can be quantified  
7 noninvasively with certain imaging methods<sup>2</sup> allowing the staging and longitudinal  
8 follow up to detect the progression or regression of a disease. For example, in the case of  
9 liver fibrosis, MRE is a validated clinical tool since it provides results comparable to liver  
10 biopsy<sup>3-6</sup> while being non-invasive and enabling the assessment of the whole liver  
11 contrary to liver biopsy which probes only a small liver sample. Indeed, MRE is now a  
12 recognized modality for the assessment of liver fibrosis stage in patients with  
13 nonalcoholic fatty liver disease (NAFLD)<sup>5,7</sup>. Many other organs targeted in clinical  
14 applications such as the heart<sup>8-10</sup>, brain<sup>11-14</sup> and breast<sup>15-18</sup> benefit also from the use of  
15 MRE as a tissue mechanical characterization technique.

16 Initially, Lewa et al.<sup>19</sup> proposed the use of mechanical waves with MRI to image the elastic  
17 properties of materials. Their method was based on the detection of Larmor frequency  
18 modulations caused by the application of mechanical waves<sup>20</sup>. Afterwards, Muthupillai et  
19 al.<sup>1</sup> proposed the application of oscillating motion encoding gradients (MEG)  
20 synchronized to the mechanical excitation to encode nuclear spins motion into the phase  
21 of the NMR signal. This technique has been largely exploited over the last decades and  
22 has become the classical strategy to carry out MRE.

23 Usually, the MEG is placed after the excitation and before signal acquisition and it  
24 oscillates at the same frequency as the mechanical excitation. Therefore, the minimum  
25 echo time TE is fixed by the duration of the MEG, resulting in a degradation of the signal  
26 to noise ratio (SNR), especially when low excitation frequencies are used on tissues  
27 having short T2 values. This effect is less important when using high excitation  
28 frequencies since the excitation periods are shorter. However, high frequencies are  
29 rapidly attenuated and the gradient system of most MRI scanners cannot reach high  
30 frequencies due to slew rate limitations.

31 The presence of oscillating MEGs complicates the use of the classical technique for some  
32 applications such as cardiac MRE, which needs short TE, low vibration frequencies and  
33 ECG triggering. This is the reason why some novel motion encoding strategies have been  
34 studied. First, the fractional encoding method introduced by Rump et al.<sup>21</sup> allowed to

1 overcome the drawback of the SNR degradation at low excitation frequencies since they  
2 proposed to use high frequency MEGs to encode them. The duration of MEG is thus  
3 shorter than the excitation wave period. This allowed the encoding of low frequencies  
4 with shorter TEs at the expense of a reduced encoding efficiency. Then, encoding  
5 strategies that do not use oscillating gradients were also proposed. For instance, a  
6 displacement encoding with stimulated echoes (DENSE) Elastography sequence<sup>22,23</sup> was  
7 proposed to encode low frequency motion in tissues exhibiting short T2 values. Short  
8 encoding gradients that are independent of the excitation wave period are used, enabling  
9 short TEs. However, the DENSE MRE strategy presents a loss of signal amplitude  
10 compared to the classical method.

11 Instead of using oscillating gradients to encode the oscillatory motion, the usage of  
12 radiofrequency (RF) field gradients was also proposed to detect motion from  
13 spectroscopic data by relating the NMR signal as a function of the wave frequency  
14 excitation<sup>24,25</sup>. This method was then validated to acquire 2D magnitude images showing  
15 shear waves propagating at frequencies in the kilohertz range in phantom experiments<sup>26</sup>.  
16 However, this method was limited in terms of RF power since a very high power was  
17 needed to obtain the desired B1 gradient.

18 More recently, the application of optimized RF pulses, designed with an Optimal Control  
19 (OC) algorithm, in presence of a constant gradient was investigated<sup>27,28</sup>. OC theory was  
20 demonstrated to be useful in MRI in the context of image contrast optimization<sup>29,30</sup> and  
21 robust excitation and refocusing<sup>31-33</sup>. Both mentioned applications are based on the NMR  
22 signal magnitude whereas in the case of MRE, OC pulses were proposed for phase  
23 contrast applications such as MRE<sup>28</sup>. The ability of such pulses to control the  
24 magnetization phase was first validated<sup>34,27</sup>. Then, it was demonstrated that the  
25 simultaneous application of an OC based pulse and a constant gradient allows the  
26 encoding of an oscillatory motion<sup>28</sup>. The pulse brings the magnetization from the  
27 equilibrium state to the desired target state that is related to the phase of the wave  
28 propagation. The OC pulse, applied with a constant gradient during the mechanical  
29 excitation, simultaneously performs spatially selective excitation and motion encoding in  
30 slice direction. As no oscillating gradients are required after the excitation, this approach  
31 enables short TE and avoids fast gradient switches, which facilitates the application of  
32 low and high frequency MRE. However, the constant gradient imposes that the motion  
33 encoding direction be similar to the slice selection direction. For now, this strategy has  
34 been applied to carry out single-frequency MRE with the above conditions<sup>35</sup>.

1 Currently, multifrequency MRE is increasingly being explored because the parameters  
2 commonly used to quantify the viscoelastic behavior of biological tissues are frequency  
3 dependent. The dispersion of the real and imaginary components of the complex shear  
4 modulus ( $G^*$ ) can provide information about the microstructure of tissues<sup>36-39</sup>. The  
5 alterations of the viscoelastic properties of tissues at a microscopic scale caused by some  
6 diseases can be detected with the dispersion results fitted to a powerlaw<sup>40-42</sup>.  
7 Multifrequency results can be acquired separately with monochromatic wave excitations  
8 at multiple frequencies or simultaneously. The simultaneous encoding of multiple  
9 frequencies was investigated by some authors. The fractional encoding method was  
10 extended to multifrequency acquisitions. It was successfully used on human liver<sup>40,43,44</sup>  
11 to simultaneously encode four sinusoidal waveforms with frequencies of 25.0, 37.5, 50.0  
12 and 62.5 Hz using a 50 Hz sinusoidal MEG. Since then, the concept of fractional encoding  
13 has been exploited in different studies to further its benefits<sup>45,46</sup>. For example, Garteiser  
14 *et al.*<sup>45</sup> proposed a MRE sequence to acquire multiple frequency components on several  
15 slices in a single examination. However, the fractional encoding method is limited to low  
16 frequency vibrations; it is thus not suitable for small samples where high frequencies are  
17 needed.

18 On the other hand, a recent study proposed a harmonic wideband encoding MRE  
19 method<sup>47</sup> using the ability of low frequency trapezoidal MEGs to encode higher  
20 frequencies, thus overcoming gradient limitations of the MR scanner. The harmonic  
21 wideband method allowed the encoding of odd multiples of the fundamental frequency.  
22 It was thus shown on phantom experiments that it could simultaneously encode 300 and  
23 900 Hz using a 300 Hz trapezoidal MEG<sup>47</sup>. Nevertheless, as the harmonic wideband  
24 encoding method is more appropriate for high frequencies, it could not be easily applied  
25 to the typical targeted organs in MRE such as the liver since the high frequency shear  
26 wave component would be rapidly attenuated.

27 These simultaneous multifrequency MRE strategies allow the reduction of the total  
28 examination time compared to the classical method encoding where only one frequency  
29 is encoded per acquisition. Despite this, the limitation imposed by the presence of the  
30 oscillating gradients remains. Hence, being able to simultaneously encode several  
31 vibrations covering a large range of frequencies without the application of MEG while  
32 reducing the examination duration could be an important added value to MRE methods.  
33 In response to this proposal, we redesigned the OC algorithm applied to MRE in order to  
34 extend the motion encoding strategy to more than one frequency component. Therefore,

1 the aim of this study is to validate the use of OC RF pulses to simultaneously encode a  
2 dual-frequency shear wave at short TE. Phantom experiments were carried out to  
3 validate the applicability of the proposed approach on a preclinical 7T MRI system. A  
4 good agreement of the shear storage modulus values was found when compared to  
5 classical monofrequency MRE experiments.

## 6 7 8 **2. OPTIMAL CONTROL THEORY**

### 9 **2.1 Optimal Control algorithm**

10 Through the application of the Pontryagin Maximum Principle (PMP)<sup>48</sup>, Optimal Control  
11 theory enables the computation of the control parameter and the associated optimal  
12 trajectory of a dynamic system with respect to a defined target state and its associated  
13 cost function. The numerical approach used to solve this optimal control problem is the  
14 GRAPE (GRAdient Ascent Pulse Engineering) algorithm which is a gradient ascent  
15 algorithm introduced for Nuclear Magnetic Resonance pulse design<sup>49</sup>. This algorithm  
16 updates the control parameter and the trajectories that satisfy the optimal conditions to  
17 minimize the cost function at each iteration, while satisfying the constraints imposed by  
18 the PMP.

19 The dynamic system in the case of MRI corresponds to the macroscopic magnetization  $\vec{M}$   
20 of isochromats, whose evolution can be modelled by Bloch equations. The control  
21 parameter corresponds to the components of the RF pulse ( $\vec{U} = (u_x, u_y)$ ), which will  
22 manipulate the macroscopic magnetization from a given steady state to the desired target  
23 state.

24 The target states are defined by the user depending on the application. For instance, they  
25 can be defined so as to optimize the magnitude of the macroscopic magnetization while  
26 ensuring the robustness of the pulse on a  $B_0$  inhomogeneity range<sup>29</sup>. Likewise, they can  
27 be defined as phase patterns so as to manipulate the phase of the macroscopic  
28 magnetization in the case of phase contrast mechanisms such as MRE<sup>27</sup>.

### 29 30 **2.2 Optimal Control applied to multifrequency MRE**

31 To perform MRE with OC, the RF pulse is simultaneously applied with a constant gradient  
32  $G_z$  to perform slice selection through the frequency selectivity of the RF pulse as it is  
33 classically done. Figure 1a presents the setup and coordinate system considered for the  
34 definition of the multifrequency MRE optimal control problem. In the optimization

1 problem, we discretize J isochromats along the slice direction (taken to be z here). Each  
2 one is located at a position  $z_{(j)}$ . This implies the concept of bandwidth of the optimized  
3 RF pulse that is related to the desired slice thickness ( $\Delta z_{in}$ ). Two outbands ( $\Delta z_{out}$ ) are also  
4 considered (Fig. 1b) with a different target state. The RF pulse and a constant gradient  
5 are simultaneously applied during the propagation of the shear wave through the  
6 phantom, which induces a time varying  $B_0$  field for all considered isochromats. The  
7 encoding motion direction is thus imposed by the gradient direction and must be parallel  
8 to it. Isochromats are then discretized along an arbitrary wavelength direction  $x_{(i)}$  (taken  
9 to be x here). Each one is described in terms of phase by  $\theta_{(i)} = 2\pi \frac{x_{(i)}}{\lambda}$ , which is  
10 independent to the propagation direction. In a previous study, it was demonstrated that  
11 considering only two isochromats separated by a quarter of a wavelength ( $\theta_{(1)} = 0$  and  
12  $\theta_{(2)} = \pi/2$ ), it is possible to converge towards a pulse that continuously encodes the  
13 wave propagation in the magnetization phase while also reducing the computation  
14 time<sup>27</sup>. In the present study, only these 2 isochromats are considered (Fig. 1c). In the case  
15 of multifrequency MRE, a shear wave composed of K different frequency components ( $f_k$ )  
16 propagates through the phantom. Therefore, in order to adapt the algorithm to  
17 multifrequency MRE, we discretized also isochromats according to their excitation  
18 frequency. For this, we considered isochromats at K different frequencies. This made the  
19 optimization process more complex since the number of controlled isochromats was K  
20 times greater and there was no guarantee that such a pulse could be found.  
21 Taking all this into account, the field variation perceived by isochromats located at (i,j) is  
22 given by:

$$23 \quad \Delta B_{0_{(i,j)}}(t) = G_z \left( \sum_{k=1}^K [A_k \sin(2\pi f_k t + \theta_{(i)})] + z_{(j)} \right) \quad (1)$$

24 where  $A_k$  represents the amplitude of each component of the shear wave. This expression  
25 of the resonance offset is included in Bloch equations for the optimization process.

26  
27 Different target states are attributed whether the isochromat is located inside ( $\Delta f_{in}$   
28 corresponding to  $\Delta z_{in}$ ) or outside ( $\Delta f_{out}$  corresponding to  $\Delta z_{out}$ ) the bandwidth. The target  
29 state for isochromats outside corresponds to the equilibrium state so as to have a proper  
30 slice selection. For the isochromats inside, the target state maximizes the transverse  
31 magnetization with a magnetization phase which is directly linked to the position of the



1 isochromat along the wavelength of the oscillatory motion they are undergoing. The  
 2 target states are thus defined by the following coordinate vectors:

$$\begin{aligned}
 3 \quad \vec{T}_{(i,j)} &= (\rho \cos \theta_{(i)}, \rho \sin \theta_{(i)}, 0) \quad \text{if } j \in \Delta f_{in} \\
 4 \quad \vec{T}_{(i,j)} &= (0,0,1) \quad \text{if } j \in \Delta f_{out}
 \end{aligned} \tag{2}$$

5 where  $\rho$  represents the magnetization amplitude varying between 0 and 1.

6  
 7 The cost function is defined in order to be minimized during the optimization process. It  
 8 corresponds to the quadratic difference between the final magnetization states after the  
 9 application of the RF pulse  $\vec{M}_{(i,j)}(t_f)$  and the defined target states  $\vec{T}_{(i,j)}$ :

$$10 \quad C(\vec{U}) = \sum_{j=1}^J \sum_{i=1}^2 \sum_{k=1}^K \|\vec{M}_{(i,j)}(t_f) - \vec{T}_{(i,j)}\|^2 \tag{3}$$

11

12

### 13 **3. MATERIALS AND METHODS**

#### 14 **3.1 Optimal Control RF pulse generation**

15 Several RF pulses were separately optimized for different pairs of frequencies: A) 300  
 16 and 900 Hz with respective wave amplitudes of 15 and 45  $\mu\text{m}$ , B) 300 and 400 Hz with  
 17 respective wave amplitudes of 15 and 20  $\mu\text{m}$  C) 300 and 600 Hz with respective wave  
 18 amplitudes of 15 and 30  $\mu\text{m}$  and D) 400 and 600 Hz with respective wave amplitudes of  
 19 15 and 30  $\mu\text{m}$ . The amplitude of the high frequency component was increased with  
 20 respect to the lower one in order to account for the greater attenuation of high  
 21 frequencies and the reduction of the encoding efficiency of the MEG at high frequencies  
 22 with the classical method. The pulse durations were fixed to 15 ms. As the relaxation  
 23 times have to be taken into account during the optimization process, a prior knowledge  
 24 of the T2 is needed. The pulse were optimized for a T1 value of 400 ms and a T2-value of  
 25 30 ms of our phantom. The pulse amplitudes were bounded during the optimization to  
 26 94  $\mu\text{T}$  in order to respect the constraints of the coil and the RF amplifier used. Only the x-  
 27 component of the RF pulse was optimized ( $u_x$ ) thus further reducing the computation  
 28 time. The slice bandwidths  $\Delta f_{in}$  were set to 7 kHz, which corresponds to a 1 mm slice with  
 29 a gradient amplitude  $G_z=164$  mT/m. The outer bandwidth intervals  $\Delta f_{out}$  were set to  
 30  $\pm[4.5, 10.5]$  kHz yielding a transition band of  $\pm[3.5, 4.5]$  kHz. The frequency step was set  
 31 to 10 Hz and 20 Hz in the slice and the outer bandwidth, respectively. Only two  
 32 isochromats groups per wavelength (at  $\theta_{(1)} = 0$  and  $\theta_{(2)} = \pi/2$ ) were considered for

1 each frequency component. This yielded a total of 4004 different isochromats which were  
2 simulated and controlled for every RF pulse. The total duration of the optimization  
3 process for one pulse was around 137 h on a computing grid of 4-core, 2.5 GHz machines.

### 4 5 3.2 Robustness to the T2 variability

6 Biological tissues are often heterogeneous and have variable transverse relaxation times.  
7 As OC pulses are optimized for a given optimization T2 value, it is expensive in terms of  
8 computation time to generate several pulses for each specific case. The robustness of OC  
9 pulses to the variability of T2 can be evaluated by simulation. For this purpose, the OC RF  
10 pulse A was applied via the Bloch equations to several numerical phantoms with different  
11 T2 values. From these results, the simulated encoded phase  $\varphi_{sim}$  defined here as the  
12 difference between the mean phase of each isochromat group ( $\varphi_{sim} = \bar{\varphi}_{sim_{iso\ \pi/2}} -$   
13  $\bar{\varphi}_{sim_{iso\ 0}}$ ) and the simulated transverse magnetization were computed. To simulate the  
14 effect of the OC pulse when there is no mechanical excitation the pulse was also applied  
15 to the same numerical phantoms with a null motion amplitude. The simulated phase  
16 noise  $\sigma_{sim}$  was then defined as the standard deviation of the isochromats phase in the  
17 absence of motion. Finally, similarly to the experimental Phase-to-Noise ratio (PNR), the  
18 simulated  $PNR_{sim}$  was calculated as the quotient of the simulated encoded phase divided  
19 by the phase noise ( $\varphi_{sim}/\sigma_{sim}$ ).

### 20 21 3.3 MRE setup

22 Acquisitions were performed on a preclinical 7 T MRI scanner (BioSpec Bruker system,  
23 Ettlingen, Germany), with a quadrature 72 mm inner diameter volume coil in  
24 transmit/receive mode.

25 Experiments were carried out on a uniform phantom composed of 75%-standard  
26 plastisol (Plastileurre Standard, Bricoleurre, France). Relaxation times measured using a  
27 RARE (Rapid Acquisition with Refocused Echoes) sequence with different TEs and TRs  
28 gave  $[T1, T2] = [420, 35]$  ms. Previous studies confirmed that the complex modulus of  
29 plastisol phantoms can be reliably assessed using MRE<sup>50,51</sup>.

30 A piezoelectric actuator (CEDRAT Technologies) was used as mechanical transducer  
31 driver. A waveform generator (Agilent 33220A) was configured to produce the sum of  
32 two harmonic signals with the above-mentioned frequencies and amplitudes.

### 33 34 3.4 MRE acquisition

1 As the objective of this study was to compare the classical monofrequency MEG method  
2 versus the OC-based multifrequency MRE proposed here, both type of acquisitions were  
3 carried out. The used sequences were based on a conventional turbo spin-echo sequence.  
4 For the classical method, one cycle of MEG with 164 mT/m maximum amplitude was  
5 added before and after the refocusing pulse. MEG was synchronized with the mechanical  
6 excitation. For the OC method, the calculated pulses were used as excitation pulse. The  
7 OC pulse itself was synchronized with the mechanical excitation. Since the OC approach  
8 actually requires the encoding of motion parallel to the slice direction, a single direction  
9 was sensitized. Both sequences are presented in Figure 2.

10 Fixed acquisition parameters were axial slice orientation, TR=1500 ms, RARE factor = 4,  
11 single slice of 1 mm thickness, field of view =  $4 \times 4 \text{ cm}^2$ , matrix size =  $128 \times 128$ .

12 To avoid artifacts during the inversion process for the viscoelastic parameters  
13 computation, the low and high shear wave frequencies were chosen so that there were at  
14 least one and a half wavelength encoded in the propagation direction and that a  
15 wavelength contained at least nine voxels<sup>52</sup>. Therefore, taking into account the size of our  
16 phantom, some pairs of frequencies between 300 and 900 Hz were considered in this  
17 work.

18 First, monofrequency shear waves were separately encoded with the classical MRE  
19 method. Then, shear waves resulting from the sum of the two components was encoded  
20 with the OC pulses. The TE was fixed to the minimum possible for each sequence giving  
21 an effective TE of 3.9 ms for the OC MRE and 13, 10.5, 8.8 and 7.4 ms for classical MRE  
22 with 300, 400, 600 and 900 Hz, respectively.

23 The waveform generator was triggered before the beginning of each TR so as to ensure a  
24 steady-state wave propagation before the encoding. Two acquisitions with inversion of  
25 the wave polarity were done for phase images subtraction and removal of static phase  
26 offsets. Acquisitions without motion were also carried out to compute the phase noise.

27 For the monofrequency acquisitions, four equally spaced phase offsets were acquired. For  
28 the simultaneous multifrequency encoding, the number of phase offsets was adapted to  
29 the frequency pairs so as to decrease the total acquisition duration. For instance, for the  
30 pair 300 and 900 Hz we only acquired five phase offsets equally spaced over one period  
31 of 300 Hz. This does not respect the Shannon sampling theorem, but generates a  
32 controlled temporal aliasing that enables the separation of the information of both  
33 frequencies without any additional examination time<sup>47</sup>. Further details of the acquisition  
34 parameters are summarized in Table 1.

## 1 3.5 Image analysis

### 2 3.5.1 G' and G'' reconstruction

3 Raw phase images were unwrapped with a quality guided path following phase  
4 unwrapping algorithm<sup>53</sup>. The 2D displacement fields, which are proportional to the  
5 unwrapped phase, were calculated. Then, a directional filter was applied in the main  
6 propagation direction (from bottom to top). A temporal Fourier transform was applied  
7 to the displacement fields along the phase offsets direction in order to obtain the different  
8 harmonics in the frequency domain. The first harmonic was kept in the monofrequency  
9 acquisitions. In the multifrequency acquisitions two harmonics were kept corresponding  
10 to the different frequency components. For example, for the pulse A, both the first and  
11 the second harmonics were kept corresponding to the 300 and 900 Hz components  
12 respectively.

13 Then, a spatial fourth-order 2D Butterworth filter with lower and upper thresholds of  
14  $0.25$  and  $2.5 \text{ cm}^{-1}$  at 300, 400 and 600 Hz, and  $1$  and  $3.5 \text{ cm}^{-1}$  at 900 Hz was applied to  
15 filter and preserve the wavelengths of interest as much as possible<sup>3,54</sup>. The spatial filter  
16 limits were chosen based on simulations of estimated wavelength values with different  
17 cut-offs filters values (data not shown).

18 The shear storage modulus  $G'$  and the loss modulus  $G''$  at each frequency were calculated  
19 after the application of the Helmholtz equation inversion<sup>55,56</sup> to the filtered displacement  
20 fields, assuming a density of  $1000 \text{ kg/m}^3$ . Finally, a  $3 \times 3$  median filter was applied to the  
21 elastograms.

22 ROIs (Region of interest) were manually drawn excluding the phantom borders and  
23 regions where the wave propagation was not sufficient (particularly at 900 Hz). The  
24 mean and standard deviation of  $G'$  and  $G''$  were computed inside the ROIs.

25

### 26 3.5.2 PNR computation

27 PNR, which evaluates the motion encoding efficiency, was computed and compared  
28 among the different acquisitions. It was defined as the ratio between the average value  
29 (over all pixels inside the same ROIs defined for the  $G'$  and  $G''$  computation) of the phase  
30 encoding in presence of mechanical excitation ( $\Delta$ ) and the phase noise, defined as the  
31 average value of the phase encoding in the absence of motion ( $\sigma$ ):  $\text{PNR} = \Delta / \sigma$ . The phase  
32 encoding is defined as the difference of the maximal and minimal phase encoded in a  
33 same pixel along time. Phase encodings were calculated on phase images obtained after

1 the application of the inverse Fourier transform to the chosen harmonics for each  
2 frequency component.

## 5 4. RESULTS

### 6 4.1 OC pulses in the simulation framework

#### 7 4.1.1 OC pulses validation

8 The double role of the OC pulses of motion encoding and slice selection can be verified by  
9 simulation and experimentally. In Figure 3, we present the characteristics of the OC RF  
10 pulse A. They are similar for the other OC pulses used in this study. The temporal  
11 evolution of the pulse magnitude is displayed in Figure 3a. Figure 3b presents the final  
12 states of the transverse magnetization in the transverse plane of the Bloch sphere of all  
13 the isochromats considered in the optimization process. The 0 and  $\pi/2$  phase  
14 isochromats are perfectly distinct. The mean phase of each isochromat group is calculated  
15 to compute the simulated encoded phase. Ideally, it should be equal to  $\pi/2$ . Isochromats  
16 outside the bandwidth can be identified as the group in the center of the graphic. It can  
17 be noticed however that the isochromat dispersion from the target state is more  
18 important than in the slice bandwidth. Figure 3c shows the simulated slice profile,  
19 calculated by integrating the transverse magnetization inside pixels aligned along the  
20 slice gradient direction. Figure 3d shows the experimental slice profile, obtained with a  
21 RF profile sequence. The resolution parameters were the same in the simulation of the  
22 profile and in the experimental RF profile: same number of points (128) and FOV (40  
23 cm). In both figures, the dashed lines represent the controlled slice thickness and  
24 outbands. The experimental slice profile matches the simulated one and the obtained  
25 slice thickness corresponds to the desired one (1 mm).

#### 27 4.1.2 Robustness to the T2 variability

28 Figure 4 shows the obtained results when the numerical phantom T2 varies between 5  
29 and 90 ms with and optimized T2 set to 30 ms. Figure 4a and 4b present the final states  
30 on two numerical phantoms of T2 values of 5 and 90 ms, respectively, with and without  
31 motion. We can observe that when there is no mechanical excitation, the two isochromats  
32 populations have a similar phase encoding resulting in a constant phase image. Figure 4c  
33 shows the quantified results in terms of simulated transverse magnetization in the slice  
34 and PNR. The transverse magnetization amplitude increases monotonously with T2 with

1 a sharp increase when  $T2 < T2_{opt}$  and a slower increase for  $T2$  values above  $T2_{opt}$ . PNR  
2 has maximum value when  $T2 = T2_{opt}$  and decreases very slightly when  $T2 > T2_{opt}$ .  
3 However, an abrupt decrease is noticed when  $T2 < T2_{opt}$ .

4

## 5 **4.2 Phantom acquisitions**

6 Figures 5a,b show, respectively, the phase and magnitude images of the dual-frequency  
7 excitation encoded with the OC RF pulse C optimized for 300 and 600 Hz. Then, figure 5c  
8 shows the phase images of the two frequency components obtained after the application  
9 of the temporal Fourier transform, choice of the harmonics and application of the inverse  
10 Fourier transform. Finally, figure 5d shows the  $G'$  elastograms for each excitation  
11 frequency. Even if some artifacts can be seen on the edges of the phantom, both vibrations  
12 components are correctly encoded. The maps for the remaining frequencies are quite  
13 uniform as expected since the phantom is supposed to be homogeneous.

14 The classical monofrequency MRE method is compared to the OC strategy in terms of  
15 phase encoding and PNR. Results are summarized in Table 1. The values of phase  
16 encoding are higher with the dual-frequency OC strategy for all the tested frequencies.  
17 This is especially favorable for the high frequency components, where the phase encoding  
18 is reduced with the classical method. However, the phase noises are also higher with the  
19 OC strategy, yielding PNR values of the same order of magnitude but usually higher than  
20 those found with the classical method.

21 The mean values and standard deviation of  $G'$  obtained for all the excitations frequencies  
22 with the classical and the OC RF pulses are presented in Figure 6. Storage modulus values  
23 found in mono and (multifrequency) acquisitions were equal to  $21 \pm 2.9$  (pulse A:  $21 \pm 3.8$ ,  
24 pulse B:  $20.8 \pm 4$ , pulse C:  $20.9 \pm 4.6$ ) kPa at 300 Hz;  $21.4 \pm 1.5$  (pulse B:  $21.4 \pm 3.2$ , pulse D:  
25  $21.6 \pm 3.2$ ) kPa at 400 Hz;  $25.4 \pm 2.6$  (pulse C:  $25 \pm 1.9$ , pulse D:  $25.1 \pm 1.7$ ) kPa at 600 Hz  
26 and  $27 \pm 3.9$  (pulse A:  $27.4 \pm 5.4$ ) kPa at 900 Hz. Loss modulus values found in mono and  
27 (multifrequency) acquisitions were  $5.7 \pm 2.2$  (pulse A:  $3.8 \pm 4.9$ , pulse B:  $4 \pm 3.9$ , pulse C:  
28  $4.6 \pm 2.2$ ) kPa at 300 Hz;  $6.4 \pm 1.5$  (pulse B:  $6.4 \pm 3.8$ , pulse D:  $6.9 \pm 3.2$ ) kPa at 400 Hz;  
29  $8 \pm 2.7$  (pulse C:  $8.5 \pm 2.9$ , pulse D:  $8.5 \pm 1.1$ ) kPa at 600 Hz and  $10.8 \pm 4.1$  (pulse A:  
30  $12.2 \pm 4.2$ ) kPa at 900 Hz.

31

## 5. DISCUSSION

This proof of concept proposes a novel method to carry out simultaneous multifrequency MRE. RF pulses, designed via the OC theory, are applied with a constant gradient while the shear wave propagates through the sample and have the double role of spatial selection and motion encoding. We validated on phantom experiments the ability of OC-based pulses to simultaneously encode two frequencies. We chose four different pairs of frequencies so as to cover the whole spectrum of excitation frequencies adapted to our phantom (between 300 and 900 Hz). Unlike the classical MEG MRE method, oscillating gradients are not needed after the application of the RF pulse. This implies the elimination of the constraints of the classical method due to the presence of MEGs such as high frequency oscillations and long TEs with low frequency vibrations. Hence, the OC approach is not limited in terms of frequency. However, the fast attenuation of high frequencies mechanical waves remains a physical limitation, especially for soft and deep-lying tissues. The OC MRE strategy was already demonstrated in the simpler case of single-frequency excitation<sup>28</sup>, hence we built upon these previous results to apply OC MRE to a dual-frequency excitation to further its benefits.

Compared to the existing simultaneous multifrequency MRE methods, with the OC approach the frequency components are not limited either to odd harmonics (harmonic wideband encoding<sup>47</sup>) or a narrow range of frequencies (fractional encoding<sup>44</sup>). Any pair of frequencies could be theoretically considered in the pulse optimization enabling exploration of the appropriate frequency range depending on the characteristics of the tissue of interest. Being able to simultaneously encode any pair or even more than two frequencies without a degraded PNR would be a valuable tool for multifrequency MRE. The sampling method could be adapted to the driving frequencies in order to minimize the total acquisition time by using non-respecting Shannon samplings<sup>47</sup> or even irregular sampling methods such as the Sequential Backward Selection (SBS) algorithm<sup>57</sup>. For instance, in the case of the 300-900 Hz multifrequency acquisition, a non-respecting Shannon sampling that produces a controlled frequency aliasing could be applied. It allowed to considerably reduce the number of phase offset to be acquired and thus acquisition time. Conventionally, at least 4 phase offsets equally spaced along the harmonic cycle are acquired to encode a monofrequency shear wave. This means that to separately encode two different frequencies we would need 8 phase offsets versus only 5 phase offsets with our proposed method. This method therefore enables a 38%

1 reduction in acquisition time to encode these 2 frequencies. However, taking into account  
2 the characteristics of our phantom, not all frequency pairs could be encoded with such an  
3 undersampling method and so the acquisition time could not always be reduced that  
4 much.

5  
6 According to the results, the dual-frequency OC acquisitions can produce higher PNR  
7 values compared to the classical monofrequency acquisitions, as previously found with  
8 monofrequency OC pulses<sup>28</sup>. A good agreement of the shear storage modulus  $G'$  obtained  
9 through the different acquisitions is also found. Nevertheless, the loss modulus were  
10 underestimated for 300 and 900 Hz in some of the multifrequency acquisitions. This  
11 could be due to the fact that the 300 Hz wavelength is big compared to the phantom size  
12 and the 900 Hz component is rapidly attenuated. In a previous study<sup>47</sup> the shear storage  
13 and loss modulus were measured by using multifrequency MRE in our phantom. It was  
14 found that  $G'(300\text{Hz}) = 20.3 \pm 2.2$ ,  $G'(900\text{Hz})=23.9 \pm 2$ ;  $G''(300\text{Hz})=6.5 \pm 2.8$ ,  
15  $G''(900\text{Hz})=7.9 \pm 3.8$ . The actual values are of the same order of magnitude but slightly  
16 higher, this could be explained because the mechanical properties of the phantom varies  
17 as it grows older (more than a year passed between the mentioned paper and the actual  
18 study).

19  
20 The RF slice profiles showed in Figure 3c,d present an imperfect null transverse  
21 magnetization beyond the controlled bandwidth and outbands rendering multi-slice  
22 acquisitions complicated. It could be possible to apply a low-pass filter with a cutoff  
23 frequency equal to the maximum value of  $\Delta z_{\text{out}}$  to reduce the effect of the pulse to the  
24 magnetization trajectories lying beyond the controlled bandwidth and outbands. However,  
25 post-filtering higher frequency components of the RF pulse has a detrimental effect on  
26 the transverse magnetization in the selected slice. Increasing the length of the outbands  
27 would allow the reduction of the transverse magnetization outside the slice but this  
28 would result in longer computation time.

29 As no oscillating gradients are required, the readout can be applied immediately after the  
30 pulse, allowing shorter echo times. Therefore, contrary to the classical method, the OC  
31 MRE approach would allow the encoding of motion in tissues with short transverse  
32 relaxation times. In this study, a spin-echo scheme was used but the application of a non-  
33 Cartesian readout is also under investigation<sup>58</sup>. Using a radial acquisition scheme would  
34 allow an even shorter echo time and would ultimately expand the application of



1 multifrequency MRE to ultra-short T2 tissues, such as tendons or ligaments. Relaxation  
2 times are taken into account during the optimization process. Indeed, the OC algorithm  
3 tries to compensate the T2 relaxation to maximize the transverse magnetization at the  
4 end of the pulse. In Figure 4c, the resulting transverse magnetization when  
5  $T2 = T2_{opt} = 30$  ms is about 80% of the maximum value even though the pulse duration is  
6 15 ms. Such a transverse magnetization can only be obtained because during the pulse  
7 duration, the magnetization trajectory corresponds to a succession of partial flips and  
8 phase encodings. Moreover, with the OC pulses we are not limited in terms of excitation  
9 frequency. High frequencies could be applied to quantify the mechanical properties of  
10 hard tissues like cartilage<sup>59</sup> to detect some diseases such as osteoarthritis<sup>60</sup>. But we could  
11 also encode low frequency vibrations with short TEs in soft tissues such as the liver.

12  
13 One limitation of the proposed approach is that a prior knowledge of some of the  
14 acquisitions parameters is needed to compute the OC pulse. Some of them are related to  
15 the RF coil (maximal amplitude), the phantom (T1 and T2 relaxations times), the MRI  
16 scanner (gradient maximum amplitude) and the mechanical excitation (amplitudes and  
17 frequencies). An incorrect correspondence between experimental and optimization  
18 parameters can affect the efficacy of the OC pulse, especially in the case of a dual-  
19 frequency pulse where the optimization process is more complex. The effect of the  
20 deviation of the experimental parameters has been investigated with simulations for  
21 some of these parameters: from figure 4, we concluded that it is still possible to encode  
22 motion when the actual T2 is bigger than the optimized T2. One can also note that for T2s  
23 that are slightly smaller than the optimized value, the OC pulse is still able to fulfill correct  
24 phase encoding but transverse magnetization rapidly decreases. It was therefore  
25 demonstrated the robustness of OC pulses to the sample T2 variability, meaning that an  
26 OC pulse optimized for a minimum possible T2 could be used in a wide range of higher  
27 T2s. This would facilitate the use of the OC strategy on clinical setups since just a few  
28 pulses could be sufficient for different applications. From simulations (data not shown  
29 here), we found that the phase is still encoded when the experimental amplitudes are  
30 smaller than the amplitudes used for the optimization. This means that OC pulses can  
31 encode the attenuation along the sample. However, having experimental amplitudes  
32 bigger than the optimization one could prevent the encoding of motion. Therefore, the  
33 amplitude of vibrations has to be fixed carefully for the optimization process and in such  
34 a way that the highest experimental amplitude is below the optimization one.

1 For the moment, we validated the use of OC RF pulses to perform multifrequency MRE in  
2 preclinical experiments where higher gradients are available. However, OC RF pulses  
3 could also be adapted to clinical requirements. We optimized some RF pulses with  
4 gradient amplitudes of the order of magnitude of clinical gradient systems ( $<40$  mT/m).  
5 Such pulses were tested in our 7T MRI scanner and demonstrated their ability to encode  
6 a dual-frequency shear wave. This confirmed that the application of OC RF pulses to  
7 encode motion is not limited by the strength of the gradient system. Furthermore, as any  
8 pair of frequencies can be considered in the optimization, it could be easily adapted to  
9 the clinical elastography frequency range. The physical limitation of higher attenuations  
10 at high frequencies could be overcome with a mechanical actuator using centrifugal force.  
11 Such an actuator was demonstrated to provide sufficiently large wave actuation at high  
12 frequencies (from 50 Hz to 80 Hz at 3 T)<sup>61</sup>. Vibration frequencies intrinsic to the MRI and  
13 the sequence should be evaluated before the transfer of the OC strategy on a clinical MRI  
14 scanner to adapt the vibration frequencies and the sampling strategy. Finally, the actual  
15 limitation of the OC pulses to only encode oscillatory motion vibrating in the same  
16 direction as the constant gradient is under investigation to expand the strategy to 3D  
17 motion encoding.

18

19 In conclusion, this article is the proof of concept of an innovative simultaneous  
20 multifrequency MRE method in a preclinical context. OC pulses have proven to be a  
21 valuable tool to encode a dual-frequency motion without the need of oscillating motion  
22 encoding gradients. Even if this novel approach presents some limitations, it is still  
23 advantageous for multifrequency MRE thanks to the resulting shorter acquisition time  
24 and achieved short echo times. We have shown that with OC pulses, a dual-frequency  
25 motion can be encoded and the viscoelastic parameters quantified, with comparable  
26 results to the classical MRE method. Future work will focus on expanding the motion  
27 encoding to more than one direction and applying the OC strategy with radial readouts  
28 to perform MRE in very short T2 tissues. Preclinical *in vivo* studies will be conducted on  
29 small animals in order to evaluate the encoding efficiency of the OC simultaneous  
30 multifrequency MRE approach.

31

32

1           **6. CONCLUSION**

2 This article presents an alternative strategy to the current simultaneous multifrequency  
3 MRE methods: applying a designed OC pulse with a constant gradient, it is possible to  
4 encode a shear wave composed of low and high frequency components without a  
5 degradation of the encoded phase. This strategy can be combined with an undersampling  
6 method in order to reduce the total acquisition time. The multifrequency OC approach  
7 could allow the mechanical characterization of short T2 tissues as it is compatible with  
8 short echo times and it could also be useful to explore the dispersion of viscoelastic  
9 parameters of tissues on a large frequency range. Further work is envisaged to  
10 investigate the preclinical applications of the presented method.

11

12

13           **DATA AVAILABILITY**

14 The datasets generated during and/or analyzed during the current study are available  
15 from the corresponding author on reasonable request.

16

## 1 REFERENCES

- 2
- 3 1. Muthupillai, R. *et al.* Magnetic resonance elastography by direct visualization of  
4 propagating acoustic strain waves. *Science* **269**, 1854–1857 (1995).
- 5 2. Greenleaf, J. F., Fatemi, M. & Insana, M. Selected Methods for Imaging Elastic  
6 Properties of Biological Tissues. *Annu. Rev. Biomed. Eng.* **5**, 57–78 (2003).
- 7 3. Yin, M. *et al.* Assessment of Hepatic Fibrosis With Magnetic Resonance Elastography.  
8 *Clin. Gastroenterol. Hepatol.* **5**, 1207-1213.e2 (2007).
- 9 4. Rouvière, O. *et al.* MR Elastography of the Liver: Preliminary Results. *Radiology* **240**,  
10 440–448 (2006).
- 11 5. Hsu, C. *et al.* Magnetic Resonance vs Transient Elastography Analysis of Patients With  
12 Nonalcoholic Fatty Liver Disease: A Systematic Review and Pooled Analysis of  
13 Individual Participants. *Clin. Gastroenterol. Hepatol.* **17**, 630-637.e8 (2019).
- 14 6. Huwart, L. *et al.* Magnetic Resonance Elastography for the Noninvasive Staging of  
15 Liver Fibrosis. *Gastroenterology* **135**, 32–40 (2008).
- 16 7. Tapper, E. B. & Loomba, R. Noninvasive imaging biomarker assessment of liver  
17 fibrosis by elastography in NAFLD. *Nat. Rev. Gastroenterol. Hepatol.* **15**, 274–282  
18 (2018).
- 19 8. Sack, I., Rump, J., Elgeti, T., Samani, A. & Braun, J. MR elastography of the human heart:  
20 Noninvasive assessment of myocardial elasticity changes by shear wave amplitude  
21 variations. *Magn. Reson. Med.* **61**, 668–677 (2009).
- 22 9. Kolipaka, A., Araoz, P. A., McGee, K. P., Manduca, A. & Ehman, R. L. Magnetic resonance  
23 elastography as a method for the assessment of effective myocardial stiffness  
24 throughout the cardiac cycle. *Magn. Reson. Med.* **64**, 862–870 (2010).
- 25 10. Elgeti, T., Beling, M., Hamm, B., Braun, J. & Sack, I. Cardiac Magnetic Resonance  
26 Elastography. *Invest. Radiol.* **45**, 6 (2010).
- 27 11. Kruse, S. A. *et al.* Magnetic resonance elastography of the brain. *NeuroImage* **39**, 231–  
28 237 (2008).
- 29 12. Green, M. A., Bilston, L. E. & Sinkus, R. *In vivo* brain viscoelastic properties measured  
30 by magnetic resonance elastography. *NMR Biomed.* **21**, 755–764 (2008).
- 31 13. Sack, I., Beierbach, B., Hamhaber, U., Klatt, D. & Braun, J. Non-invasive measurement  
32 of brain viscoelasticity using magnetic resonance elastography. *NMR Biomed.* **21**,  
33 265–271 (2008).

- 1 14. Murphy, M. C. *et al.* Decreased brain stiffness in Alzheimer's disease determined by  
2 magnetic resonance elastography. *J. Magn. Reson. Imaging* **34**, 494–498 (2011).
- 3 15. Sinkus, R. *et al.* High-resolution tensor MR elastography for breast tumour detection.  
4 *Phys. Med. Biol.* **45**, 1649–1664 (2000).
- 5 16. Sinkus, R. *et al.* Viscoelastic shear properties of in vivo breast lesions measured by MR  
6 elastography. *Magn. Reson. Imaging* **23**, 159–165 (2005).
- 7 17. Lorenzen, J. *et al.* MR elastography of the breast: preliminary clinical results. *RöFo -*  
8 *Fortschritte Auf Dem Geb. Röntgenstrahlen Bildgeb. Verfahr.* **174**, 830–834 (2002).
- 9 18. McKnight, A. L. *et al.* MR Elastography of Breast Cancer: Preliminary Results. *Am. J.*  
10 *Roentgenol.* **178**, 1411–1417 (2002).
- 11 19. Lewa, C. J. Magnetic Resonance Imaging in the Presence of Mechanical Waves.  
12 *Spectrosc. Lett.* **24**, 55–67 (1991).
- 13 20. Lewa, C. J. & Certaines, J. D. de. MR imaging of viscoelastic properties. *J. Magn. Reson.*  
14 *Imaging* **5**, 242–244 (1995).
- 15 21. Rump, J., Klatt, D., Braun, J., Warmuth, C. & Sack, I. Fractional encoding of harmonic  
16 motions in MR elastography. *Magn. Reson. Med.* **57**, 388–395 (2007).
- 17 22. Robert, B., Sinkus, R., Gennisson, J.-L. & Fink, M. Application of DENSE-MR-  
18 elastography to the human heart. *Magn. Reson. Med.* **62**, 1155–1163 (2009).
- 19 23. Strasser, J., Haindl, M. T., Stollberger, R., Fazekas, F. & Ropele, S. Magnetic resonance  
20 elastography of the human brain using a multiphase DENSE acquisition. *Magn. Reson.*  
21 *Med.* **81**, 3578–3587 (2019).
- 22 24. Karczmar, G. S., Tweig, D. B., Lawry, T. J., Matson, G. B. & Weiner, M. W. Detection of  
23 motion using B1 gradients. *Magn. Reson. Med.* **7**, 111–116 (1988).
- 24 25. Baril, N. *et al.* MR Detection of Mechanical Vibrations Using a Radiofrequency Field  
25 Gradient. *J. Magn. Reson.* **154**, 22–27 (2002).
- 26 26. Turk, E., Ider, Y. Z., Ergun, A. S., Demir, T. & Atalar, E. Shear Wave Imaging by using B1  
27 gradients. in *Proc Int Soc Magn Reson Med; 2013; abstract 0015*.
- 28 27. Lefebvre, P. M. *et al.* Active control of the spatial MRI phase distribution with optimal  
29 control theory. *J. Magn. Reson.* **281**, 82–93 (2017).
- 30 28. Van Reeth, E. *et al.* Constant gradient elastography with optimal control RF pulses. *J.*  
31 *Magn. Reson.* **294**, 153–161 (2018).
- 32 29. Van Reeth, E. *et al.* Optimal control design of preparation pulses for contrast  
33 optimization in MRI. *J. Magn. Reson.* **279**, 39–50 (2017).

- 1 30. Van Reeth, E., Ratiney, H., Lapert, M., Glaser, S. J. & Sugny, D. Optimal control theory  
2 for applications in Magnetic Resonance Imaging. *Pac. J. Math. Ind.* **9**, (2017).
- 3 31. Conolly, S., Nishimura, D. & Macovski, A. Optimal Control Solutions to the Magnetic  
4 Resonance Selective Excitation Problem. *IEEE Trans. Med. Imaging* **5**, 106–115  
5 (1986).
- 6 32. Skinner, T. E. *et al.* New strategies for designing robust universal rotation pulses:  
7 Application to broadband refocusing at low power. *J. Magn. Reson.* **216**, 78–87  
8 (2012).
- 9 33. Kobzar, K., Ehni, S., Skinner, T. E., Glaser, S. J. & Luy, B. Exploring the limits of  
10 broadband 90° and 180° universal rotation pulses. *J. Magn. Reson.* **225**, 142–160  
11 (2012).
- 12 34. Gershenzon, N. I. *et al.* Linear phase slope in pulse design: Application to coherence  
13 transfer. *J. Magn. Reson.* **192**, 235–243 (2008).
- 14 35. Sango Solanas, P. *et al.* Constant gradient magnetic resonance elastography  
15 experiments on phantom and bovine liver. in *Proc Int Soc Magn Reson Med; 2019;*  
16 *abstract 683*.
- 17 36. Guo, J. *et al.* Fractal network dimension and viscoelastic powerlaw behavior: II. An  
18 experimental study of structure-mimicking phantoms by magnetic resonance  
19 elastography. *Phys. Med. Biol.* **57**, 4041–4053 (2012).
- 20 37. Bigot, M. *et al.* The apparent mechanical effect of isolated amyloid- $\beta$  and  $\alpha$ -synuclein  
21 aggregates revealed by multi-frequency MRE. *NMR Biomed.* **33**, (2020).
- 22 38. Posnansky, O. *et al.* Fractal network dimension and viscoelastic powerlaw behavior:  
23 I. A modeling approach based on a coarse-graining procedure combined with shear  
24 oscillatory rheometry. *Phys. Med. Biol.* **57**, 4023–4040 (2012).
- 25 39. Jugé, L. *et al.* Microvasculature alters the dispersion properties of shear waves - a  
26 multi-frequency MR elastography study: Microvasculature Alters the Dispersion  
27 Properties of Shear Waves. *NMR Biomed.* **28**, 1763–1771 (2015).
- 28 40. Asbach, P. *et al.* Viscoelasticity-based Staging of Hepatic Fibrosis with Multifrequency  
29 MR Elastography. *Radiology* **257**, 80–86 (2010).
- 30 41. Wuerfel, J. *et al.* MR-elastography reveals degradation of tissue integrity in multiple  
31 sclerosis. *NeuroImage* **49**, 2520–2525 (2010).
- 32 42. Sack, I., Jöhrens, K., Würfel, J. & Braun, J. Structure-sensitive elastography: on the  
33 viscoelastic powerlaw behavior of in vivo human tissue in health and disease. *Soft*  
34 *Matter* **9**, 5672 (2013).

- 1 43. Klatt, D., Hamhaber, U., Asbach, P., Braun, J. & Sack, I. Noninvasive assessment of the  
2 rheological behavior of human organs using multifrequency MR elastography: a study  
3 of brain and liver viscoelasticity. *Phys. Med. Biol.* **52**, 7281–7294 (2007).
- 4 44. Asbach, P. *et al.* Assessment of liver viscoelasticity using multifrequency MR  
5 elastography. *Magn. Reson. Med.* **60**, 373–379 (2008).
- 6 45. Garteiser, P. *et al.* Rapid acquisition of multifrequency, multislice and multidirectional  
7 MR elastography data with a fractionally encoded gradient echo sequence:  
8 MULTIFREQUENCY MRE WITH GRADIENT ECHOES. *NMR Biomed.* **26**, 1326–1335  
9 (2013).
- 10 46. Dittmann, F. *et al.* In vivo wideband multifrequency MR elastography of the human  
11 brain and liver: In Vivo Multifrequency wMRE of the Human Brain and Liver. *Magn.*  
12 *Reson. Med.* **76**, 1116–1126 (2016).
- 13 47. Sango Solanas, P. *et al.* Harmonic wideband simultaneous dual-frequency MR  
14 Elastography. *NMR Biomed.* (2020) doi:10.1002/nbm.4442.
- 15 48. Pontryagin, L. S. *Mathematical Theory of Optimal Processes.* (CRC Press, 1987).
- 16 49. Khaneja, N., Reiss, T., Kehlet, C., Schulte-Herbrüggen, T. & Glaser, S. J. Optimal control  
17 of coupled spin dynamics: design of NMR pulse sequences by gradient ascent  
18 algorithms. *J. Magn. Reson.* **172**, 296–305 (2005).
- 19 50. Chakouch, M. K., Charleux, F. & Bensamoun, S. F. Development of a phantom  
20 mimicking the functional and structural behaviors of the thigh muscles characterized  
21 with magnetic resonance elastography technique. in *2015 37th Annual International*  
22 *Conference of the IEEE Engineering in Medicine and Biology Society (EMBC)* 6736–  
23 6739 (IEEE, 2015). doi:10.1109/EMBC.2015.7319939.
- 24 51. Lefebvre, P. M. *et al.* Comparison of viscoelastic property characterization of plastisol  
25 phantoms with magnetic resonance elastography and high-frequency rheometry. in  
26 *2016 38th Annual International Conference of the IEEE Engineering in Medicine and*  
27 *Biology Society (EMBC)* 1216–1219 (IEEE, 2016).  
28 doi:10.1109/EMBC.2016.7590924.
- 29 52. Mura, J., Schrank, F. & Sack, I. An analytical solution to the dispersion-by-inversion  
30 problem in magnetic resonance elastography. *Magn. Reson. Med.* **84**, 61–71 (2020).
- 31 53. Ghiglia, D. C. & Pritt, M. D. *Two-dimensional phase unwrapping: theory, algorithms,*  
32 *and software.* (Wiley, 1998).
- 33 54. Mariappan, Y. K., Glaser, K. J. & Ehman, R. L. Magnetic resonance elastography: A  
34 review. *Clin. Anat.* **23**, 497–511 (2010).

- 1 55. Manduca, A. *et al.* Magnetic resonance elastography: Non-invasive mapping of tissue  
2 elasticity. *Med. Image Anal.* **5**, 237–254 (2001).
- 3 56. Oliphant, T. E., Manduca, A., Ehman, R. L. & Greenleaf, J. F. Complex-valued stiffness  
4 reconstruction for magnetic resonance elastography by algebraic inversion of the  
5 differential equation. *Magn. Reson. Med.* **45**, 299–310 (2001).
- 6 57. Reeves, S. J. & Heck, L. P. Selection of Observations in Signal Reconstruction. *IEEE*  
7 *Trans Signal Proc* **43**, 788–791 (1995).
- 8 58. Sango Solanas, P., Tse Ve Koon, K., Van Reeth, E., Caussy, C. & Beuf, O. Ultra-short echo  
9 time Magnetic Resonance Elastography. in *Proc Int Soc Magn Reson Med; 2020;*  
10 *abstract 168.*
- 11 59. Lopez, O., Amrami, K. K., Manduca, A. & Ehman, R. L. Characterization of the dynamic  
12 shear properties of hyaline cartilage using high-frequency dynamic MR elastography.  
13 *Magn. Reson. Med.* **59**, 356–364 (2008).
- 14 60. Setton, L. A., Elliott, D. M. & Mow, V. C. Altered mechanics of cartilage with  
15 osteoarthritis: human osteoarthritis and an experimental model of joint  
16 degeneration. *Osteoarthritis Cartilage* **7**, 2–14 (1999).
- 17 61. Neumann, W. *et al.* A novel 3D printed mechanical actuator using centrifugal force for  
18 magnetic resonance elastography: Initial results in an anthropomorphic prostate  
19 phantom. *PLOS ONE* **13**, e0205442 (2018).

20

21



1 **ACKNOWLEDGEMENTS**

2 This work was performed within the framework of the LABEX PRIMES of University of  
3 Lyon (ANR-11-LABX-0063), within the program "Investissements d'Avenir" (ANR-11-  
4 IDEX-0007) operated by the French National Research Agency (ANR). MR experiments  
5 were acquired on the PILoT platform, member of the France Life Imaging infrastructure  
6 (ANR-11-INBS-0006).

7

8

9 **AUTHOR CONTRIBUTIONS**

10 Conception and design: P.S.S., K. TVK., E.VR., H.R., F.M., C.C., O.B.

11 Data collection: P.S.S., K.TVK, O.B.

12 Data analysis: P.S.S.

13 Manuscript drafting: P.S.S.

14 Revision of the manuscript and/or editing: P.S.S., K. TVK., E.VR., H.R., F.M., C.C., O.B.

15 All authors read and approved of the final manuscript

16

17

18 **COMPETING INTERESTS**

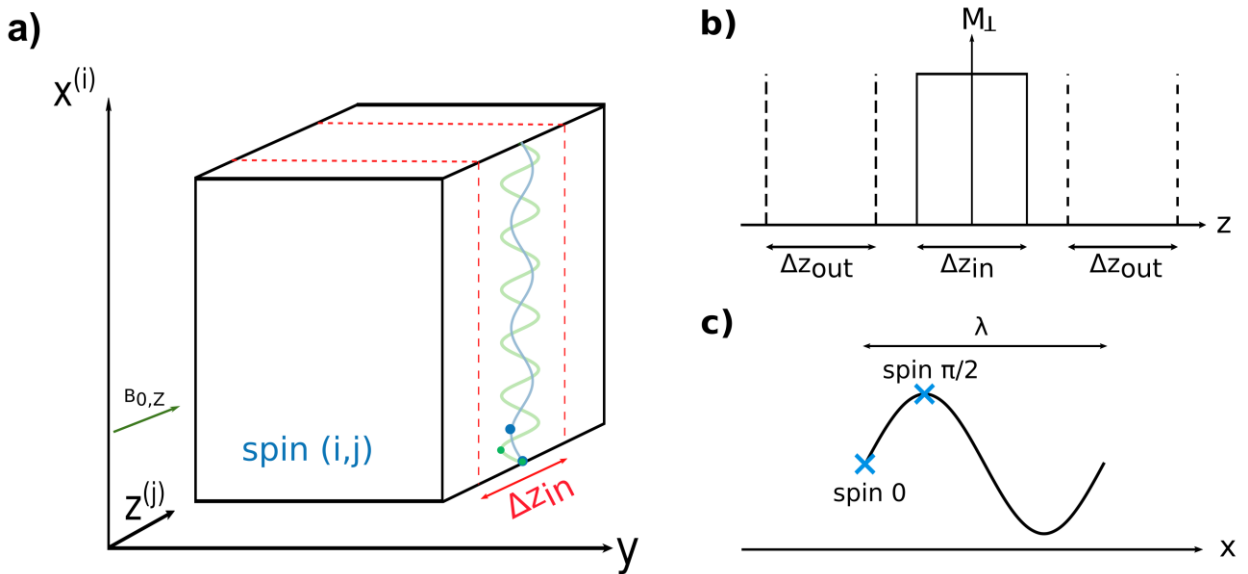
19 The author(s) declare no competing interests.

1 **Figures**

2

3 Figure 1. a) Experimental setup: the shear wave propagates in the phantom along the x-  
4 axis. The motion sensitizing direction is fixed to the slice gradient direction. b) An axial  
5 slice is acquired with a corresponding bandwidth  $\Delta z_{in}$  and controlled outbands  $\Delta z_{out}$   
6 along the z-axis, all of which are discretized. c) Isochromats are discretized along the  
7 shear wave propagation direction (x-axis) and are defined by  $\theta_i = 2\pi x_i / \lambda$  with  $x_i$   
8 representing a specific position.

9



10

11

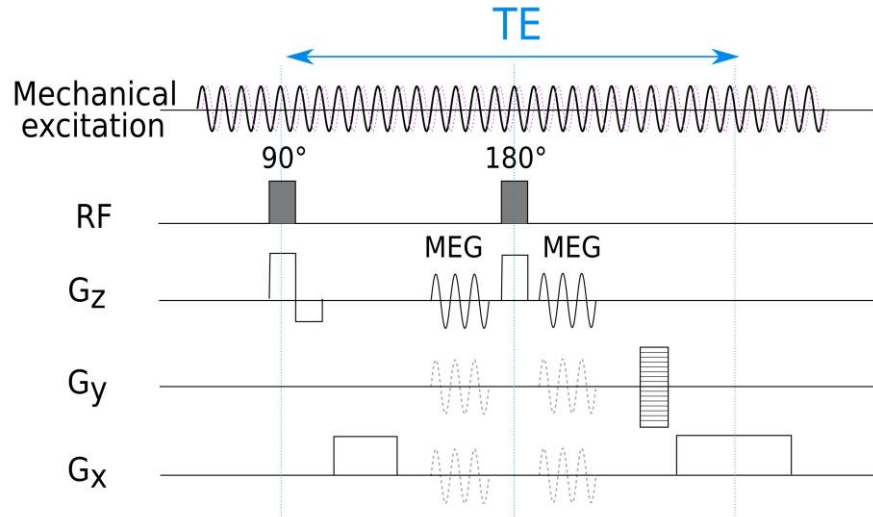
12

13

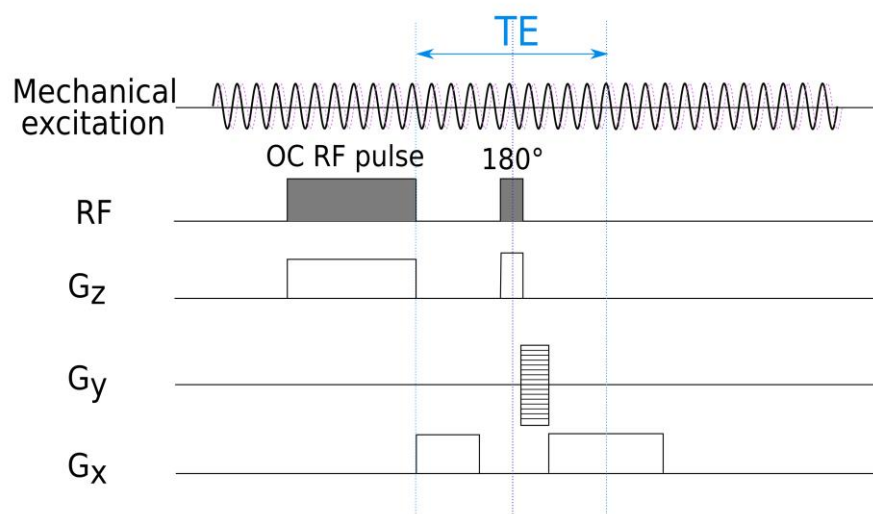
1 Figure 2. Sequence diagrams of a) the classical MEG MRE and b) the OC-based MRE used  
2 in this study.

3

**a)**



**b)**



4

5

6

7

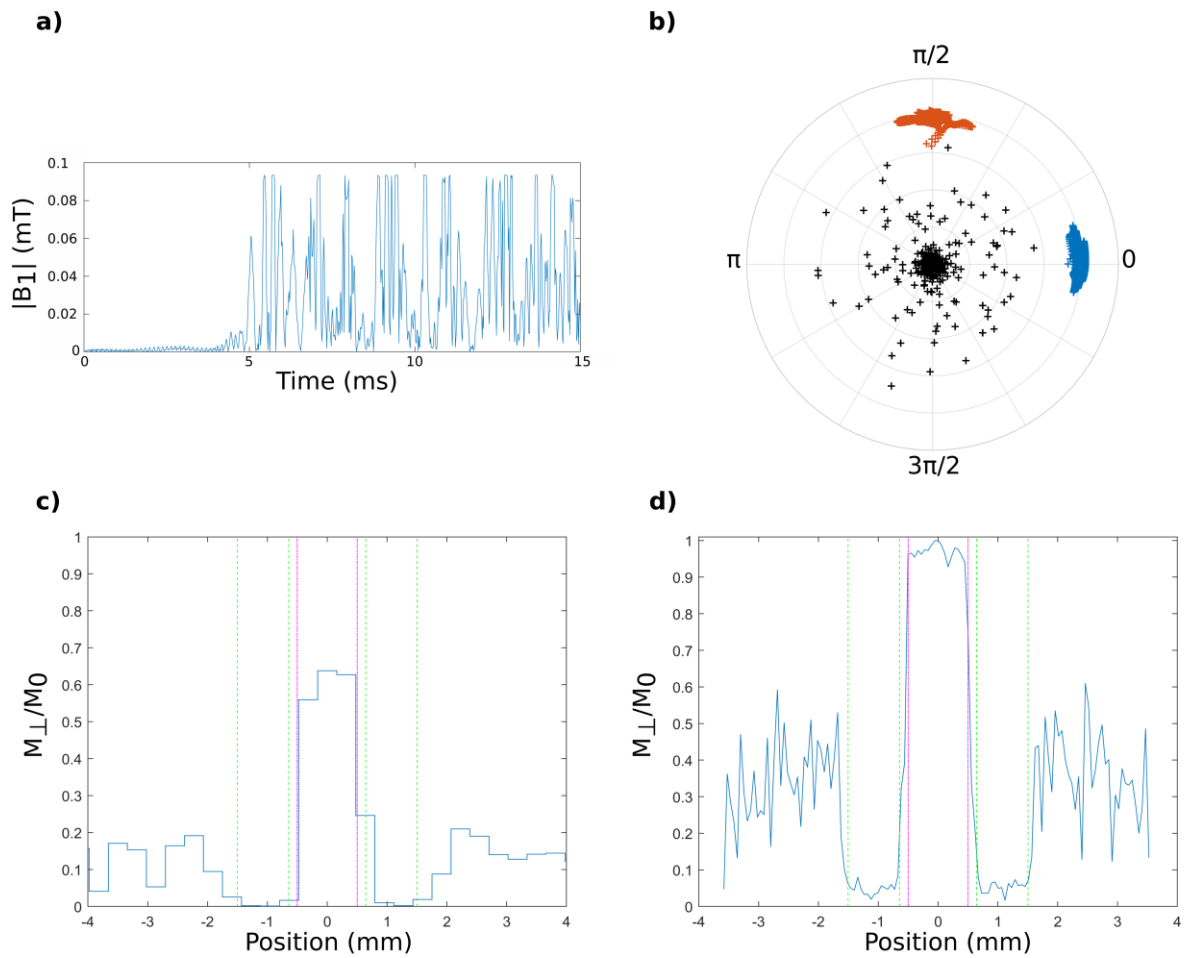
8

9

10

1 Figure 3. a) Temporal evolution of the magnitude of the OC RF pulse A ( $B_1 = u_x$ ). b) Final  
 2 transverse magnetization states in the Bloch sphere after the application of the OC pulse.  
 3 The null (blue) and  $\pi/2$  (orange) phase isochromats are perfectly distinct. c) Simulated  
 4 slice profile d) Experimental slice profile obtained with a RF profile sequence. The same  
 5 resolution parameters were used in the simulation and experimental RF profile. The pink  
 6 and green dashed lines in c and d represent the theoretical controlled slice thickness and  
 7 outbands, respectively.

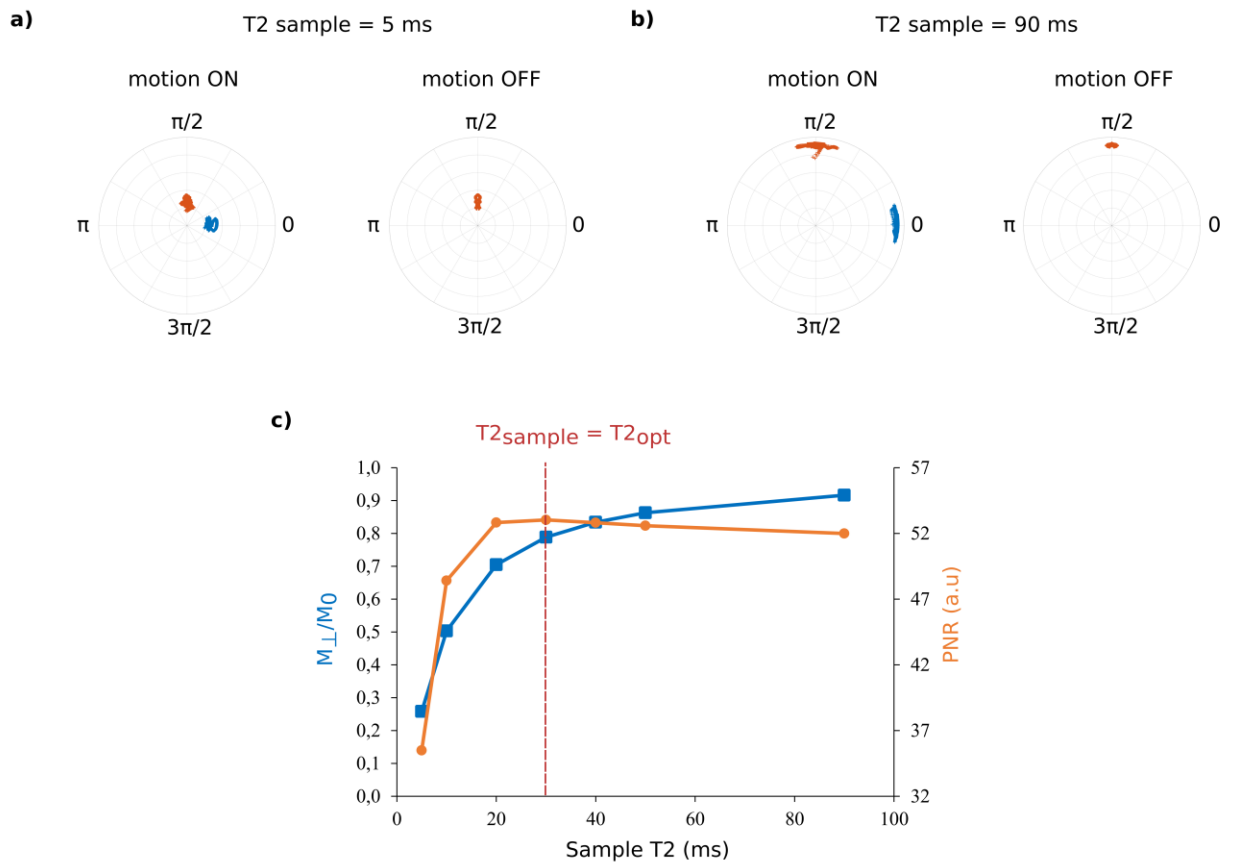
8



9

1 Figure 4. Numerical evaluation of the robustness of the OC pulse A ( $T_{2opt} = 30$  ms) with  
 2 respect to the variability of the sample  $T_2$ -value. Final transverse magnetization states  
 3 are presented in Bloch spheres when applying the OC pulse with and without motion for  
 4 samples with  $T_2$ -values of a) 5 ms and b) 90 ms. c) Simulated transverse magnetization  
 5 amplitude and PNR variation with respect to sample  $T_2$ -value.

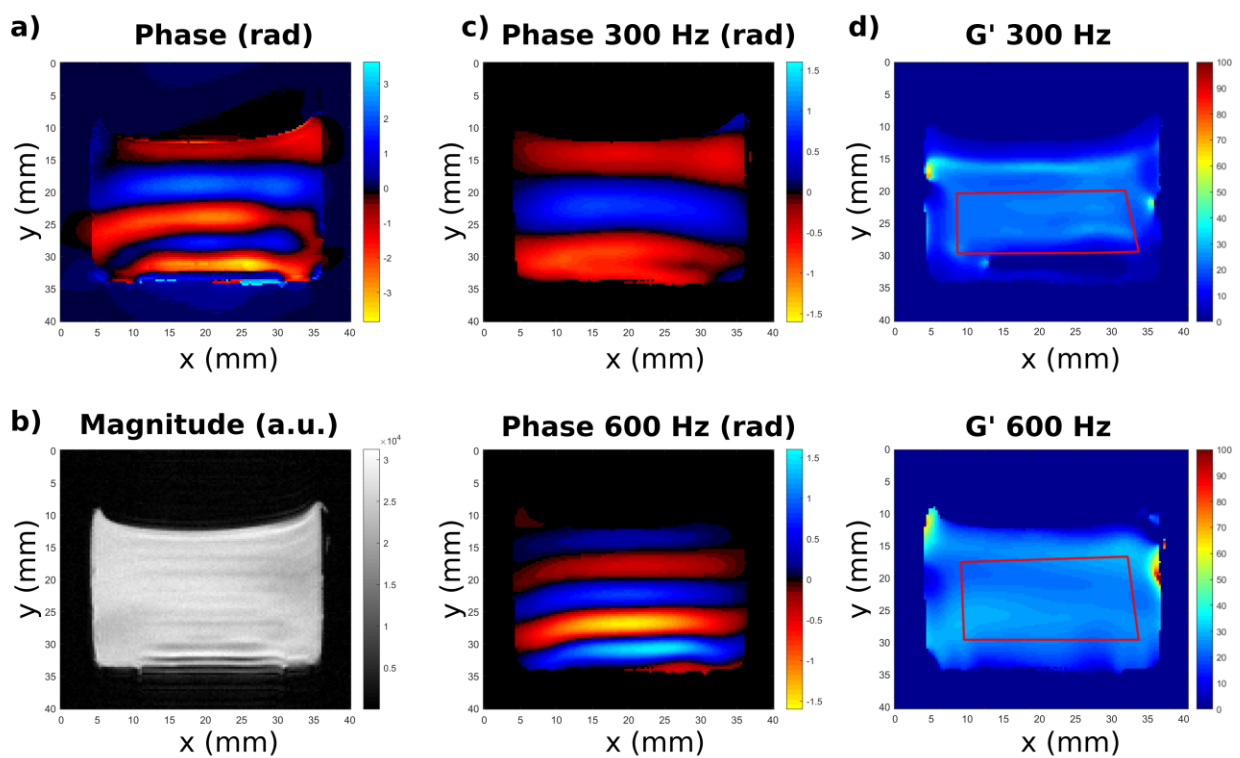
6  
 7  
 8



9

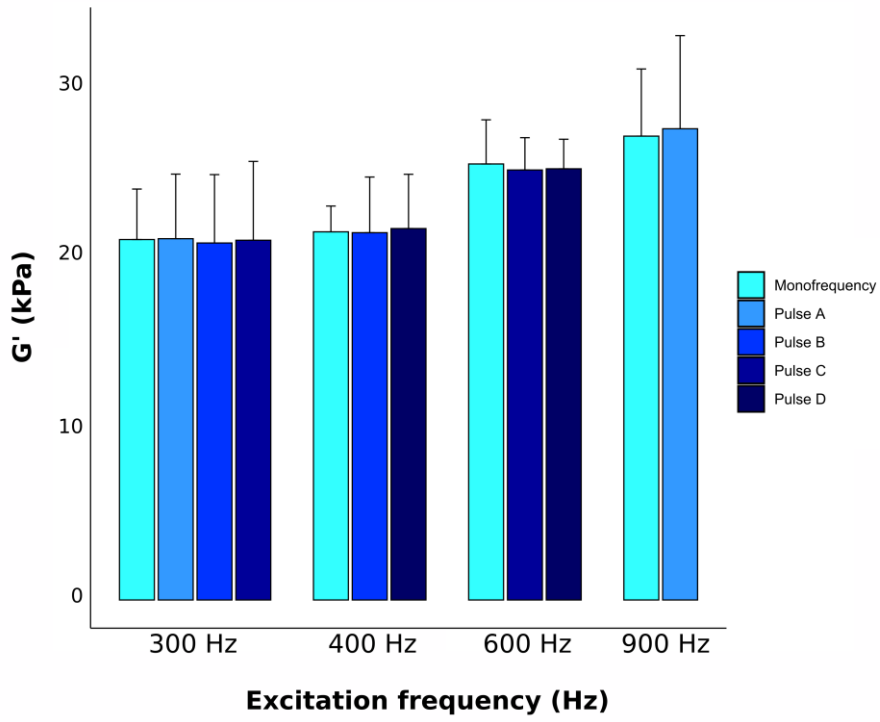
1 Figure 5. a) Phase and b) magnitude images of the composite excitation 300 Hz  
 2 and 600 Hz acquired with the OC pulse C. c) Then separated phase images (rad) of every  
 3 frequency component extracted after temporal Fourier transform, choice of the  
 4 corresponding harmonics and application of the inverse Fourier transform: top: 300 Hz;  
 5 bottom: 600Hz. d)  $G'$  elastograms (kPa) reconstructed for each frequency component:  
 6 top: 300 Hz; bottom: 600 Hz. The ROIs used for the computation of the shear storage  
 7 modulus mean and standard deviations are shown with red lines on the maps in c.

8  
 9



10  
 11  
 12  
 13

1 Figure 6. Mean values, with standard deviations displayed as error bars, of the  
2 reconstructed shear storage modulus  $G'$  for all the different excitation frequencies  
3 obtained with the classical monofrequency and the OC multifrequency methods.  
4  
5



6

1 **Tables**

2 Table 1. Acquisition parameters (frequencies  $f_k$  and amplitudes  $A_k$  of the excitation shear wave; frequency  $f_{MEG}$  and number of cycles  $N_G$  of  
 3 the MEG; echo time, number of phase offsets, frequency resolution of the sampling  $\Delta f$  and acquisition time) and results (phase encoding  $\Delta$ ,  
 4 phase error  $\sigma$  and PNRs) obtained with the different acquisition modes.

5

Acquisition	$f_k$ (Hz)	$A_k$ (V)	$f_{MEG}$ (Hz)	$N_G$	TE (ms)	#phase offsets ( $\Delta f$ )	Acquisiti on time	$\Delta_k$ (rad)	$\sigma$ (rad)	PNR <sub>k</sub>
Classical MRE	300	0.5	300	1	13	4 (300)	3' 12"	1.3	0.035	21
Classical MRE	400	1	400	1	10.5	4 (400)	3' 12"	0.46	0.037	12.4
Classical MRE	600	2	600	1	8.8	4 (600)	3' 12"	0.58	0.030	19.4
Classical MRE	900	1.5	900	1	7.4	4 (900)	3' 12"	0.05	0.027	1.9
OC MRE pulse A	300:900	0.5 :1.5	-	-	3.9	5 (300)	4'	1.6 : 0.13	0.043	36.8 : 3
OC MRE pulse B	300:400	1 :1.3	-	-	3.9	9 (100)	7' 12"	1.2 : 1.3	0.067	18.4 : 18.7
OC MRE pulse C	300:600	1 :2	-	-	3.9	5 (300)	4'	1.4 : 1.5	0.042	33.8 : 35.7
OC MRE pulse D	400:600	0.5 :1.5	-	-	3.9	7 (200)	5' 36"	2 : 1.8	0.048	41.4 : 37.3

6